Soft Matter

Microstructure and elasticity of dilute gels of colloidal discoids

Journal:	*Soft Matter*
Manuscript ID	SM-ART-11-2021-001605.R1
Article Type:	Paper
Date Submitted by the Author:	13-Dec-2021
Complete List of Authors:	Kao, Peng-Kai; University of Michigan, Chemical Engineering Solomon, Michael; University of Michigan, Chemical Engineering Ganesan, Mahesh; University of Michigan, Chemical Engineering

Microstructure and elasticity of dilute gels of colloidal discoids

Peng-Kai Kao[†], Michael J. Solomon[†, *], and Mahesh Ganesan[†, *]

[†]Department of Chemical Engineering, University of Michigan, Ann Arbor, Michigan 48109, USA

***Corresponding Authors:**

Prof. Michael J. Solomon

Address: North Campus Research Complex, Building 10 – A151, 2800 Plymouth Road, Ann Arbor, MI 48109

Phone: 734-764-3119

Email: mjsolo@umich.edu

Dr. Mahesh Ganesan

Address: North Campus Research Complex, Building 20 –106W, 2800 Plymouth Road, Ann Arbor, MI 48109

Phone: 734-546-0210

Email: maheshg@umich.edu

Abstract

The linear elasticity of dilute colloidal gels formed from discoidal latex particles is quantified as a function of aspect ratio and modeled by confocal microscopy characterization of their fractal cluster microstructure. Colloidal gels are of fundamental interest because of their widespread use to stabilize complex fluids in industry. Technological interest in producing gels of desired moduli using the least number of particles drives formulators to produce gels at dilute concentrations. However, dilute gels self-assembled from isotropic spheres offer limited scope for rheological tunability due to the universal characteristics of their fractal microstructure. Our results show that changing the building block shape from sphere to discoid yields very large shifts in gel elasticity relative to the universal behavior reported for spheres. This shift – tunable through aspect ratio – yields up to a 100-fold increase in elastic modulus at a fixed volume fraction. From modeling the results using the theory for fractal cluster gel rheology, which is applicable at the dilute conditions of this study, we reveal that the efficient generation of elasticity by the colloidal discoids is the consequence of the combined effects of shape anisotropy on the fractal microstructure of the gel network, the anisotropy of the attractive interparticle pair potentials, and the volumetric compactness of the fractal cluster. These results extend prior characterizations of the rheology of non-spherical particulate gels by providing quantitative estimates of how the specific mechanisms of fractality, pair potential, and clustering mediate the profound effects of particle shape anisotropy on the elastic rheology of colloidal gels.

1. Introduction

Colloidal gels are sample-spanning networks of particle aggregates that exhibit solid-like rheological properties such as finite elastic modulus and yield stress[1]. They are used to stabilize complex fluids in a range of industry sectors such as paints, agrochemicals and pharmaceutics by imparting a soft quiescent elasticity to the formulation [2,3]. Given their abundant consumption, industries seek to – from a viewpoint of sustainable manufacturing – produce gels of tailored elasticity by using the least number of colloidal particles. This technological need drives formulators to work with colloidal materials for gelation in the limit of dilute concentrations.

Experimentally, gels at dilute particle concentrations ($\phi \leq 0.1$) are formulated by quenching particles into strong, short-range attractive pair potentials by addition of salts or depletants [4,5]. Gelation occurs through arrested spinodal decomposition, that, at dilute conditions

and strong attractions, proceeds via diffusion limited cluster aggregation (DLCA)[6]. In this regime, the gel microstructure consists of uniformly distributed, conjoined fractal clusters[1,6]. Within the clusters, the particles are aggregated into a porous, fractal network[7]. The material property of interest to formulators is the gel linear elastic modulus, G'. In dilute fractal cluster gels, the elastic modulus is modeled as $G' \sim \kappa_0 a^{-1} \phi^{(1+\beta)/(3-d_f)}$. This well-known model, reviewed in the Results section, relates the gel elasticity to the size and spring constant of the fractal clusters[4,7,8]. Here, a is the primary particle size, κ_0 is the strength of the bond between particles making up the network, d_f is the cluster fractal dimension and β is the anisotropy of the cluster elastic backbone.

Studies have shown that the microstructure of dilute sphere gels exhibits universal characteristics; in particular, the value of their fractal dimension and backbone anisotropy are fixed. These values, as observed in gels of varying particle chemistries and interactions, as well as in computer simulations, are $d_f \approx 1.85$ and $\beta \approx 2.80 - 3.1$ [4,9–14]. The universality in microstructure fixes the power-law exponent of the $G' - \phi$ dependence. Indeed, experimental values reported for the G' vs ϕ power-law exponent in dilute DLCA sphere gels fall within 3.2 – 3.6 which is consistent with $\approx$ 3.3 – 3.6 obtained by substituting the universal values for d_f and β in the above model [13,15–17]. As a result, for dilute sphere gels, the only parameters controlling for gel G' are the volume fraction, ϕ, particle size, a and bond strength, κ_0. However, in practice, the latter two parameters, are of limited utility for rheological design, because changing the particle size alters the gelation time (e.g., a 2-fold decrease in a led to a 3-fold increase in gelation time for fluorinated latex aggregates[18]) and increasing κ_0 requires using significant concentrations of additives (e.g., generating a 2-fold increase in κ_0 for polymethacrylate particles aggregating in the presence of $MgCl_2$ required a 20-fold increase in the salt utilization[19]). These parameters are typically not used by formulators for rheological design because they are otherwise set to produce the gel's intended function. Gel rheology in the case where the building blocks are spheres is consequently primarily tuned through the particle concentration, ϕ. A consequence of this limited design space is seen in Romer et al, where, by drawing from data from multiple researchers, the authors showed that, in the dilute range $10^{-3} \leq \phi \leq 10^{-1}$, the ϕ dependence of G' of sphere colloidal gels collapses onto a universal curve when normalized by particle size [13]. It is thus desirable to identify design parameters to control gel rheology that step outside the limitations imposed by using spherical

monomers. Here, we characterize and quantify how and why introducing shape anisotropy is an effective means to expand the narrow space for design and control of dilute colloidal gel rheology.

A number of studies have characterized the rheology of gels produced from shape anisometric monomers (e.g., laponite platelets[20], boehmite rods[21], rod virus [22] and 2D colloids [23,24]). These reports collectively demonstrate that the ϕ dependence of rheological functions in non-spherical colloidal gels greatly differ from that seen for gels produced from simple spheres. For example, at a fixed concertation, aggregate networks of boehmite rods (aspect ratio, $r = 9$) showed higher yield stresses than the case in which the primary network constituents were spheres [21,25]. Moreover, when the rod aspect ratio was increased to $r = 25$, the same yield stress was obtained at 4-fold lower particle concentration. Even the microstructure of anisometric cluster gels was found to depart from the properties of sphere gels. For example, DLCA of dilute rod suspensions [14] and laponite platelets [20] were found to yield networks whose fractal dimension showed a strong dependence on the building block aspect ratio, deviating from the universal value of 1.85 seen for spheres. These findings suggest that introducing shape anisotropy could enable greater tunability of gel rheology; however, the specific microstructural and particle interactions that mediate the effect of particle shape on rheology have been neither identified nor quantitatively modeled [26,27]. This lack of a mechanistic understanding of the fundamental drivers of the shift in gel rheology due to shape anisotropy limits rheological design and translation to industry practice. Conjectures about the mechanisms have included non-central forces[22,28], anisotropy in excluded volume,[14] and increases in the number of contacts per particle[28,29].

Here, using polystyrene colloidal discoids as a model anisometric system, we build upon the prior literature to demonstrate the utility of shape anisometry in expanding the design space for gels and specifically quantify the different factors that underpin the effect of shape on dilute gel rheology. We first show that the ϕ dependence of G' in discoidal gels exhibits a remarkable shift from the universality of sphere gels as aspect ratio, r is changed. In addition to a shift of the modulus curve to very low volume fraction – discoidal gels produce the same elasticity as a sphere gel using 15 times less material – we also observe that the power-law exponent describing G' vs ϕ changes with r. Second, through application of the model for fractal cluster gel rheology and independent measurement of model parameters through confocal microscopy, we quantify the origins of this shift to be due to a multiplicative contribution of shape effects on network fractality, interparticle potential and cluster compactness. The fractal dimension and shape of the elastic

backbone in discoidal gels differs from the universal values for spheres; these differences explain the r dependence of the $G' - \phi$ power-law. The anisotropy in pair-potential increases the particle-particle spring constant, thereby generating a further shift in the elastic modulus. Finally, an additional effect of cluster compactness on gel rheology is found from the r-dependence of the scaling theory's prefactor, which itself can be inferred from the independent characterizations of rheology and microstructure we perform. Remarkably, each of these effects aligns with the others, generating the large effect of shape anisotropy on gel rheology.

This work presents a simple, efficient means for expanded design and control of the rheology of colloidal gels. In addition to its direct utility in producing and using discoid gels, the analysis reveals why shape has the effect on gel rheology that it does. This enables the translation of the results to industry practice because the mechanistic origins have been quantified, which previously was unavailable. That particle shape effects are in fact the consequence of even more fundamental, microstructural factors that are determinative of gel rheology opens the possibility that even greater rheological changes are achievable through other anisotropic shapes that impact these factors.

2. Methods and materials

2.1 Colloidal particles

The particles used in this study are polystyrene (PS) colloids. Fluorescently labeled carboxylate modified microspheres with diameter 1.00 ± 0.02 μm (F8821 FluoSpheres, Thermo Fisher Scientific, zeta potential = -52.4 ± 3.2 mV) were used for confocal microscopy experiments. Rheology experiments were performed using non-fluorescent, sulfate modified latex particles with diameter 1.00 ± 0.02 μm (S37498, Invitrogen, zeta potential = -55.6 ± 1.8 mV). The particle diameters were computed from scanning electron microscopy (SEM) images (TESCAN RISE, Michigan Center for Materials Characterization).

2.2 Thermomechanical squeezing of PS spheres

Colloidal discoids are generated by uniaxial compression of precursor polystyrene microspheres. Both the fluorescent and non-fluorescent precursor spheres are subjected to the same treatment. The method is adapted from Ahn et al[30]. The stock PS particles are thrice washed in de-ionized water and gently mixed with 10 wt% poly(vinyl alcohol) (PVA, molecular weight = 30

– 70 kDa, Sigma Aldrich) solution prepared in DI water. The choice of PVA and its concentration is based on prior work[31]. The mixture is then poured onto 35 mm petri dishes (Nunc IVF Petri Dishes, Thermo Scientific) and allowed to dry for 24 hours at 25°C on a precision leveling platform (TrippNT). After the edges are trimmed, the dried PVA films with embedded spheres are sandwiched between silicone rubber sheets (50A durometer, 0.5mm thick, McMaster Carr) and placed in between two 152 mm x 152 mm stainless steel panels (1 mm thick, McMaster Carr). See Supplemental Information (SI) Figure S1 for the setup arrangement. The composite is then placed between heated platens of a bench-top press (Model CH 4386, Carver, Inc.) at 120°C (above the glass transition temperature of polystyrene, 90°C) and at a nominal contact pressure of 180 kPa. The residence time is set to 20 minutes for the PS-PVA films to reach the setpoint temperature (determined using a thermocouple thermometer, Fisher Scientific). A uniaxial compression is then applied to deform the film in which the spheres are embedded. The force is held for 20 min, following which the heat is turned off. The pressed films are allowed to cool under pressure to room temperature. The forces applied in this study are 750, 2800, 4200 kPa.

2.3 Retrieving colloidal discoids

Discoids are retrieved from the pressed PVA films following the procedure of Madivala et al[32]. The same procedure is followed for discoids prepared for both microscopy and rheology experiments. The PS-PVA films are dissolved in a 7:3 mixture of deionized (DI) water – isopropanol at 35°C for twelve hours with vigorous stirring. The solution is then heated to 60°C for 30 min to dissolve the PVA completely. The solution is centrifuged, and the recovered particles are thrice washed in the same solvent. The particles are then dispersed in DI water and heated to 60°C for 30 min with vigorous stirring to dissolve any final traces of PVA. The particles are then thrice washed in DI water and recovered. The discoidal particles obtained are finally resuspended in DI water for usage. The concentration of particles is measured using a hemocytometer (C-Chip, SKC, Inc). The average zeta potential of the discoids is -45.3 ± 3 mV, indicating a stable suspension, similar to the seed spheres, whose zeta potential is -52.4 ± 3.2 mV (Zetasizer Nano ZSP, Malvern Instruments). Aspect ratio, r, and discoid major axis *2A* are measured from images acquired by SEM of dilute samples in which discoids lie flat on the substrate. The minor axis *2B* is then obtained from conservation of volume of the seed sphere as per Hsiao et al[33].

2.4 Gelation of colloidal particles for microscopy and rheology

For gelation studies, the particles are resuspended in a buoyancy-matching mixture of deuterium oxide (151882, Sigma-Aldrich) and DI water (resistance 18.2 MΩ, using Barnstead MicroPure UV/UF Purification System, Thermo Scientific) to prevent sedimentation effects [4]. Colloidal gels are assembled by the addition of $MgCl_2$ (68475, Sigma-Aldrich), which initiates aggregation[34]. We follow the 50-50 mixing rule where equal parts of particles in H_2O-D_2O are mixed with equal parts of $MgCl_2$ solution to yield a final solution of desired particle volume fraction and [$MgCl_2$] = 10mM.

2.5 Confocal microscopy of colloidal gels

An inverted confocal laser scanning microscope (CLSM) (Nikon A1Rsi, equipped with NA = 1.4, 100x objective, oil-immersion type) is used to image the 3D microstructures of the gels self-assembled from fluorescently labeled particles. After the addition of $MgCl_2$ solution, the suspension is briefly and gently mixed for homogeneity and loaded into a 16-well chambered cover glass (CultureWell ChamberSLIP 16, Grace Bio-Labs) mounted on the microscope stage above the objective. The chamber was closed to prevent evaporation. The gels form quiescently for 45 minutes before imaging. For visualization and microstructure characterization, 3D image volumes of size 512 x 512 pixels with pixel size 0.083 μm were acquired, beginning between 8 to 10 μm above the coverslip. The image stacks comprised of ~ 200 slices spaced at 0.083μm. Thus, the top of the image volume is located 25 to 27 μm above the coverslip. While acquiring image volumes, the intensity gain was gradually increased in the z-direction in steps of 1 unit for every 0.5 μm to compensate for the loss of image intensity at depths greater than 8 μm due to the refractive index mismatch between polystyrene particles and H_2O-D_2O solution. CLSM visualization of the purified discoids are observed to be free of self-aggregation prior to the start of gelation (SI Figure S2).

2.6 Box-counting image analysis to compute fractal dimension

The fractal dimension, d_f, of each gel network is computed from confocal micrographs using the box counting method implemented as a custom MATLAB program[35,36]. Raw CLSM images are subjected to a thresholding filter of value S to distinguish foreground and background pixels. Segmented image volumes are then divided into cubes of dimension L x L x L (pixel^3) (c.f.

Figure 4(a))[36,37]. The value of L is systemically varied from L = 2 pixels to L = 64 pixels. At each step, the number of cubes ($N(L)$) needed to cover all the foreground pixels corresponding to the gel is counted. Gel d_f is then obtained from the power-law fit $N(L) = c_1(L/I)^{-d_f}$. Here, I is the image size (in pixels) and c_1 is a proportionality constant.

To address the S dependence inherent to this method, we apply the criteria of Thill and co-workers[35]. First, we vary S from 0 to 255 and plot d_f versus S as shown in SI Figure S3. The optimal threshold – where d_f does not change significantly – is identified by fitting the data to a third order polynomial and identifying the point where the concavity of the curve is zero. The optimal thresholds, found to be S = 136, 144, 152 and 141 for r = 1, 0.42, 0.20 and 0.09 respectively, were then used to compute the d_f values reported in Figure 4. This analysis accounts for any differences in instrument settings for image acquisition used due to batch-to-batch variation in particle fluorescence intensities.

To test the fidelity of this method, a complementary approach to identify the optimal threshold was followed. First, the d_f of sphere gels was determined from their radial distribution function, g(r_0) [38]. Here, g(r_0) is computed from particle centroids using tools available in TRACKPY[39] and FREUD[40] Python libraries. g(r_0) describes the average number of particles at a distance r_0 from a basis particle, relative to that of an ideal gas. For fractal structures, $g(r_0) \sim r_0^{d_f - 3}$ for $r_0/2A > 3$ [41,42]. Following this equation, the fractal dimension is obtained from the slope of the log-log plot of g(r_0) data (SI Figure S4). This method yields d_f = 1.87 ± 0.02 for sphere gels. Second, this value is matched with SI Figure S3 to find the threshold at which the d_f values for sphere gels match. A value of S = 138 is identified, which is consistent with the numbers identified above. The d_f for all the discoid gels were then computed at this threshold value. Across the range of aspect ratios studied, the relative standard deviation in d_f computed using the two methods is less than 2.5%, thus validating the box-counting method.

These data are acquired in a volume extending from approximately 10 μm above the bottom boundary. This corresponds to 10 major axis diameters for spheres, and – for the most extreme discoid aspect ratio – 5 major axis diameters. We assessed any potential effects of the proximate boundary on the fractal property characterizations (such as d_f) by checking for potential differences in fractal properties across the image volume for the specific case of the sphere gels. The confocal image volume of a sphere gel was divided into two equal stacks: one for the bottom

half of the gel and other for the top half. Each stack is of height ~ 8 microns (see SI Figure S5). The g(r_0) analysis is applied to both image volumes and the results compared to that obtained for the full image volume. The overlap of the g(r_0) curves and the statistical similarity of the computed d_f of each volume with that of the full volume suggests that any wall effects on the gel microstructure are less than the resolution of the fractal dimension characterization itself (SI Figure S5).

2.7 Skeletonization image analysis to compute backbone topography

The backbone of sphere and discoid gels was extracted from confocal image volumes following the method of Immink et al[43,44] and Kollmannsberger et al[45]. Raw confocal images were first pre-processed by applying a standard Gaussian blur (cubic kernel of size 5 voxels) to filter out noise and subsequently binarized using Otsu's method[46]. Morphological closing was then performed (cubic structural element of size 1 voxel) that removed discretization noise followed by the removal of small unconnected structures (components of volume < 1% of the largest connected component in the image). These processes were implemented using the 3D Volumetric Image Processing Toolbox available in MATLAB. The pre-processed image volumes were then skeletonized using the medial axis thinning algorithm, available through the *bwskel* function in MATLAB to produce a voxel thick backbone of the gel network[47].

The backbone dimension, d_B and anisotropy, ϵ were then computed as per the following post-processing steps. The skeleton was cleaned and converted into a non-directed weighted graph of nodes and edges using the open-source image-processing add-on to MATLAB, *Skel2Graph3D*[48]. The length, l and coordinates of the shortest connected path between all node pairs were then extracted using Dijkstra's algorithm available in MATLAB as part of their Graph and Network Algorithms function libraries. Euclidian distances, r_E between node pairs were directly computed from their coordinates on the skeleton. Coordinates of the shortest path was then used to compute their center of mass radius of gyration, r_g as well as their radius of gyration projected onto a plane perpendicular to their end-to-end axis, $r_\perp$. Then, d_B and ϵ were obtained through fits to the measured data as $l = c_2 r_E^{d_B}$ and $r_\perp^2 = c_3 r_g^{2\epsilon}$ [9,10,49,50]. Here, c_2 and c_3 are proportionality constants.

Potential effects of the near boundary on d_B and ϵ were assessed by the same method used for the fractal dimension. First, the image volume of a sphere gel was divided into two half-

volumes – top and bottom. Second, the skeletonization procedure was applied to each stack (see SI Figure S6). The d_B and ϵ for the half-volumes were statistically similar to that obtained for the full volume. The analysis shows that boundary effects on the microstructural properties of the gel skeleton are small for the imaging heights used here.

2.8 Rheological characterization of colloidal gels

Rheological measurements are performed with a stress-controlled rheometer (Discovery Hybrid Rheometer-3, TA Instruments) using a 40 mm stainless steel parallel plate geometry and a Peltier temperature-controlled plate (TA Instruments). Roughness 600 grit sandpaper (Part # 47185A51, McMaster Carr) was attached to both the top and bottom geometry surface to prevent wall slip[51]. The sample gap was set to be 500 μm. The temperature for all the rheology measurements is set to 20°C. Suspensions were loaded onto the Peltier plate, the top geometry was lowered, and particles were allowed to quiescently assemble at the measurement gap for a gelation time of 45 minutes. An insulated solvent trap cover (TA Instruments) was used to prevent evaporation. Gel rheology was then measured by performing oscillatory strain amplitude sweeps ranging from $\gamma = 10^{-4}$ to 10^{-1} at a constant oscillation frequency of 1 rad/s.

We checked that the above choice of sandpaper and gap addressed any potential wall slip and confinement effects by performing measurements for sphere gels using different roughness sandpapers and geometry gaps (SI Figure S7). The relative standard deviation of these measurements for linear storage modulus, G' is less than 10% indicating the results are independent of choice of measurement setup[52]. Instrument sensitivity limits on the strains sweep plots (Figure 2) were determined by performing experiments with aqueous solutions of PEO (molecular weight ~ 1 x 10^6 g/mol, Sigma Aldrich) at 2.0, 2.5, 3.0 and 4.0 wt% (prepared in DI water) to determine the lower stress limits of the rheometer (SI Figure S8).

3. Results

3.1 Colloidal gels assembled from discoids of different aspect ratios

Discoids used in this study are prepared by thermo-mechanical compression of spheres[30]. We use colloidal discoids because recent progress in this fabrication technique yield uniformly sized colloids in quantities sufficient for rheometry[30]. The discoid shape is furthermore common in engineered[53] and living systems[54]. The seed polystyrene microspheres (diameter $2A$ = 1.00

± 0.02 μm), embedded in a polymer film, were subjected to uniaxial compression at pressures of 750, 2800 and 4200 kPa (c.f. Methods, SI Figure S1) yielding discoids with aspect ratio, $r = (B/A)$ = 0.42 ± 0.01, 0.20 ± 0.01 and 0.09 ± 0.03 respectively. The major axes for these particles are $2A$ = 1.34 ± 0.02 μm (for r = 0.42), 1.72 ± 0.01 μm (for r = 0.20) and 2.23 ± 0.04 μm (for r = 0.09); the corresponding minor axis are $2B$ = 0.56 ± 0.01 μm, 0.35 ± 0.01μm and 0.21 ± 0.01 μm. A single batch of this fabrication process, which takes about 1.5 days per batch, yields enough discoids to perform about 5 rheology experiments at a gel volume fraction of ϕ = 0.01 with the

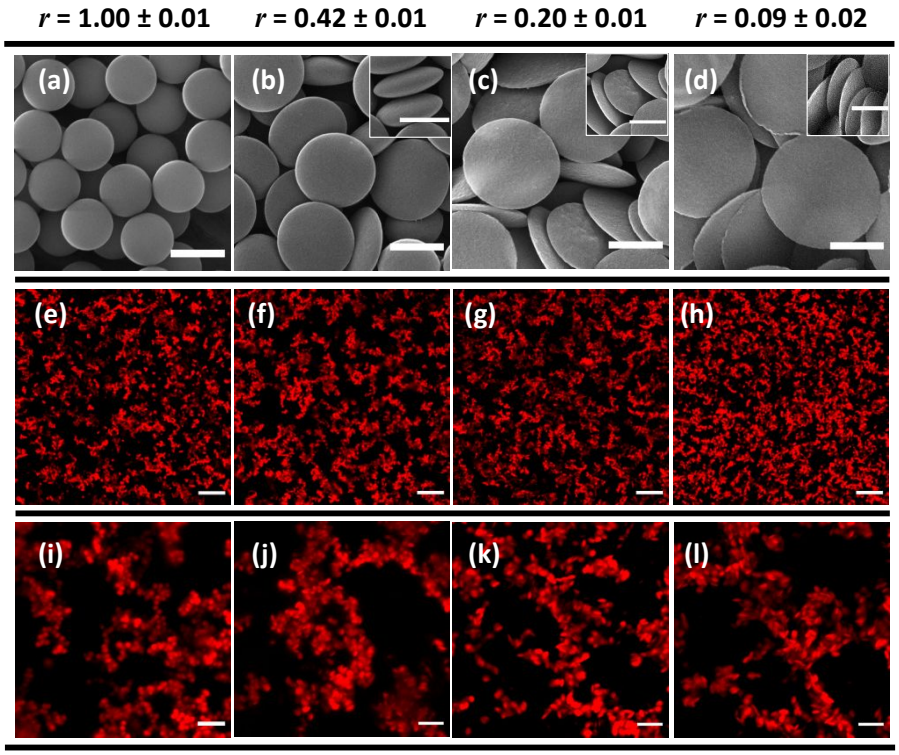

Figure 1. (a-d) Representative SEM images of colloidal particles with aspect ratio r = 1, 0.42, 0.20, and 0.09 respectively. Insets of different viewing angles show the thickness of the discoids. Scale bars for (a-d) are 1 μm. (e-l) Confocal projections (Δz = 20μm) of colloidal gels with aspect ratio r = (e,i) 1.0, (f,j) 0.42, (g,k) 0.20 and (h,l) 0.09. Here, colloid volume fraction ϕ = 0.015, concentration of $MgCl_2$ is 10mM. The scale bars for (e-h) are 20μm and (i-l) 5μm.

rheometer setup used in this study (40 mm parallel plate fixture at a measurement gap of 0.5 mm, c.f. Methods). Figure 1(a)-(d) show scanning electron micrographs of the seed spheres and the as fabricated discoids. Insets in Figure 1(b)-(d) provide an orthogonal view; the shape uniformity and successive flattening of the spheroidal shape of the particle with decreasing aspect ratio is

apparent. We observed that, a very small number of discoids (less than 1 in 50) at r = 0.20 and (less than 2 in 50) r = 0.09 had minor curling at their edges.

Particles were suspended in a density-matched mixture of H_2O-D_2O and gelation was induced by addition $MgCl_2$ to a final concentration of 10mM [34]. The salt screens surface charges promoting short-range van der Waals attractions that drive gelation through a DLCA process [34]. Figure 1(e)-(l) compares maximum projections of the three-dimensional structure of the self-assembled colloidal gels at particle volume fraction of ϕ = 0.015. Here, images in Figure 1(i)-(l) are zoomed in regions of the micrographs in Figure 1(e)-(h). Researchers working with gels formed by discotic clay minerals have described the microstructure as being a 'house-of-cards' network; however, from visual inspection, we here see little evidence for such structures in Figure 1[53]. Instead, a hierarchical, self-similar, fractal microstructure is apparent for both the sphere (r = 1) and discoid (r = 0.09 – 0.42) gels. The heterogeneous, inter-connected microstructures that span the image space at intermediate length scales (Figure 1(e)-(h)) are seen to persist even at smaller length scales (Figure 1(i)-(l)). This description is consistent with the well-known fractal cluster architecture of dilute colloidal gels[4]. In addition, the gels formed by discoids possess a microstructure (Figure 1(j)-(l)) that is interspersed with both condensates – aggregates with no orientational ordering – and strands – particles with a face-to-face orientational alignment. This mixture of partially ordered and disordered aggregates is similar to the configuration reported by Hsiao et al. for discoids assembled through depletion forces[33]. The formation of percolated gel networks at similar volume fractions was also reported for salt-induced aggregation of laponite platelets (r = 0.03 – 0.04) [20], boehmite rods (r = 3.9 – 30) [28] and silica rod colloids (r = 10) [55].

3.2 Elasticity shift in discoid gels

Figure 2 plots oscillatory shear rheological measurements performed on dilute gels produced from spheres (r = 1) and discoids (r = 0.20) at varying particle concentrations. Corresponding measurements for r = 0.42 and r = 0.09 discoidal gels are included in the Supplemental Information Figure S9. In the volume fraction range studied here, both sphere and discoid gels exhibit similar functional dependence of gel elastic modulus (G') on oscillatory shear strain amplitude (γ): a linear regime with plateau elasticity at low strain amplitudes ($\gamma < 0.003$) followed by an onset of non-linearity and a rapid drop in modulus with increasing strain amplitude (Figure 2(a)-(b), SI Figure S9). The tan(δ) – defined as the ratio of viscous to elastic modulus – is

about 0.20 in the linear regime and increases to values > 1 in the non-linear regime (inset in Figure 2 and SI Figure S9). The finite G' and tan(δ) < 1 together indicate a solid-like, elastically dominated response, characteristic of physical gels. At higher strain amplitudes, the rapid loss of

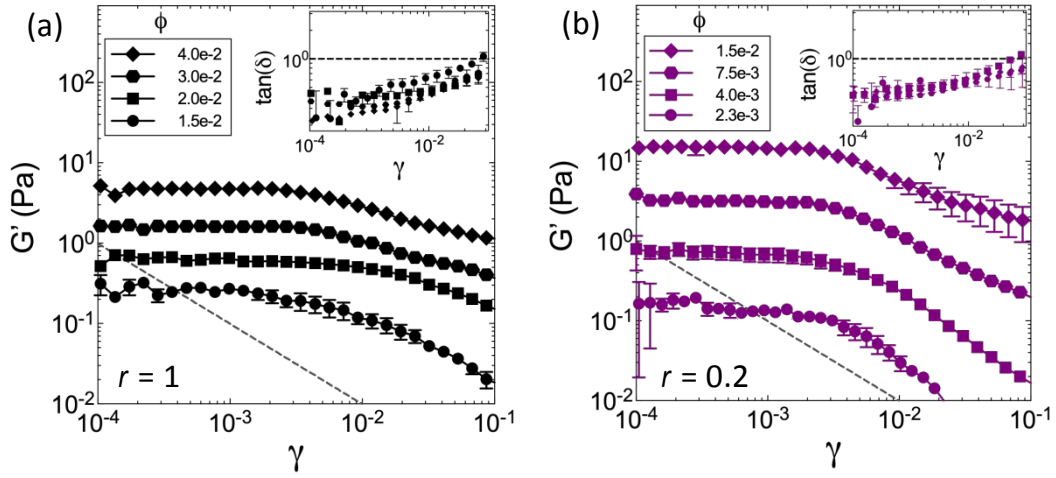

Figure 2. Storage modulus, G' and (inset) tan(δ) as a function of strain amplitude, γ for colloidal gels made from (a) spheres (r = 1) and (b) discoids (r = 0.2). The oscillation frequency is 1 rad/s. The dashed line indicates the instrument sensitivity limits (c.f. Methods). The concentration of $MgCl_2$ is 10mM.

elasticity and the cross-over between G' and the loss modulus, G'' (c.f. SI Figure S12), represents a fluidization transition[52].

Extreme differences between discoidal and spherical gels are seen by plotting the dependence of their linear G' on particle volume fraction, ϕ (Figure 3). The reported G' is an average over the linear region in Figure 2, which is identified as the strain amplitudes less than the point at which G' deviates by 5% from its maximum value[7]. First, we observe elastic rheology in discoid gels at a volume fraction that is more than an order of magnitude lower than spheres. For instance, sphere gels display G' = 0.2 Pa at ϕ = 1.5 x 10^{-2} while gels consisting of r = 0.20 and r = 0.09 discoids already exhibit similar elasticity at ϕ = 2.3 x 10^{-3} and 1.1 x 10^{-3} respectively. Relatedly, discoidal gels exhibit between 10^1–10^2-fold higher elastic modulus than spherical gels at fixed volume fraction, with level of stiffening increasing with anisotropy. For example, at ϕ = 1.5 x 10^{-2}, G' = 0.17 Pa and 18 Pa for sphere and r = 0.20 discoid gels, respectively. At ϕ = 7.5 x 10^{-3}, gel modulus increases by 20-fold as discoid anisometry increases from r = 0.42 to 0.09.

Second, we find that the exponent, Π, describing the ϕ dependence of G', $G' \sim \phi^{\Pi}$, decreases as Π= 3.53 ± 0.16, 2.93 ± 0.10, 2.52 ± 0.05 and 2.15 ± 0.15 for r = 1, 0.42, 0.2 and 0.09 respectively. These differences in the power law behavior are statistically significant (one-way ANOVA yields p = 0.0048). The value Π = 3.53 for the spheres agrees with previous reports, which average Π = 3.51 ± 0.15 [4,13]. The slower growth in elastic modulus with volume fraction for the anisotropic gels – as represented by the decreasing power law – is in itself noteworthy and agrees with the shear rheology of rod[21,22] and platelet clay gels[56]. For instance, the elastic modulus in laponite clay gels scaled with particle concentration with a power-law exponent of ~2.3 and gels of rodlike virus exhibited an exponent of ~2.5 [22] – both of which are lower than the value seen for dilute sphere gels. In addition to this feature, the power law curve of the elastic modulus itself shifts to progressively lower volume fractions with aspect ratio, culminating with a shift of 22.4 ± 5.5 at

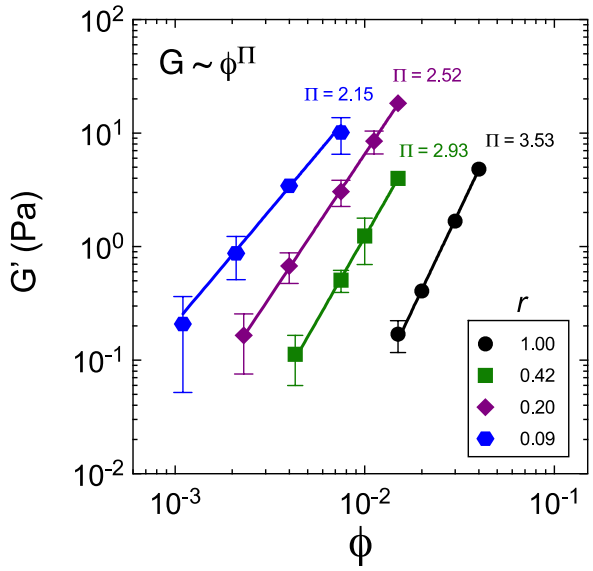

Figure 3. The dependence of linear storage elastic modulus, G' on particle volume fraction, ϕ for colloidal gels made from spheres (r = 1) and discoids (r = 0.42, 0.20 and 0.09). The uncertainties in the exponents are ± 0.15, ± 0.05, ±0.10 and ±0.16 for r = 0.09, 0.20, 00.42 and 1.00 respectively. At some data points, error bars are not visible because they are small relative to the marker size.

the lowest discoid aspect ratio. Figure 3 therefore shows that the shifts in pre-factor and exponent combine to generate very large absolute effects of shape anisotropy on the rheology of dilute colloidal gels.

Early studies on dilute particulate gels produced from anisometric monomers, such as clay minerals [57] and boehmite rods [28] also reported deviations in mechanical properties relative to

spheres. For instance, flocculated suspensions of attapulgite clay ($r \sim 0.05$) exhibited equivalent elastic modulus at volume fractions 5-fold lower than that measured for gels of spherical latex colloids[57]. Similarly, the arrested localization lengths in dilute DLCA gels of boehmite rods (r = 3.9) was 10^2-fold lower than that measured for spheres at same ϕ. From a microrheological perspective, a decrease in localization length is consistent with an inverse increase in rod gel elasticity relative to spheres. Therefore, through experimentation at various discoidal aspect ratios and volume fractions, Figure 3 specifically quantifies the utility of anisometric monomers for expanding the range of gel elastic modulus that can be produced at these dilute conditions. However, previously, the specific physical parameters that underly these remarkable differences in gel rheology were not known. In the subsequent sections we will address and quantify the multiple, microscale effects that are mediated by the discoidal particle shape and which combine multiplicatively to determine gel rheology.

3.3 Model to investigate mechanism of the elasticity shift

To develop an explanation for the aspect ratio dependence of the shift in discoidal gel elasticity, we apply a well-known theory for dilute colloidal gel rheology developed by Shih et al[7] and further extended by de Rooij et al[8] and Krall and Weitz[4]. Briefly, in this microelastic model, the gel is described as a uniform packing of fractal clusters. The characteristic cluster size, R_c, is set by the particle volume fraction, $R_c \sim V_p^{1/3} \phi^{-1/(3-d_f)}$, where V_p is the hard particle volume[4]. The gel elastic modulus is then determined by the spring constant, $\kappa(R_c)$ of these clusters: $G' \sim \kappa(R_c)/R_c$. The spring constant of the cluster is determined by the bending rigidity of its skeletal backbone – a fractal chain of particles spanning the length of the cluster[58]. Relatedly, $\kappa(R_c)$ is given as $\kappa(R_c) \sim \kappa_0 R_c^{-\beta}$, where κ_0 is the bending constant of the bond between a pair of particles within the cluster and β is determined by the fractal structure of the cluster spanning backbone. Specifically, $\beta = 2\epsilon + d_B$, where d_B is the backbone fractal dimension and ϵ represents the anisotropy of the backbone[8]. The model prediction for G' is then given as:

$$G'(\phi,r) = f\kappa_0 V_p^{-\frac{1}{3}} \phi^{\frac{1+\beta}{3-d_f}} \quad (1)$$

Equation (1), applicable in the dilute limit ($\phi < 0.1$)[8], describes a power-law dependence of G' on ϕ. The pre-factor of the scaling is determined by three parameters. They are: κ_0, V_p and, f – a proportionality constant. The power-law exponent depends on d_f and β, which together describe the hierarchical microstructure of the gel. The characteristic length scale in equation (1) has been taken as $V_p^{1/3}$, rather than the particle radius, in anticipation of our applying the model to anisometric particles[29,59].

The model is generally applicable to gel materials with fractal cluster structure; it does not prescribe the shape of the gel's constituent particles [13]. As a consequence, it has been widely used to model the rheology of dilute gels formed from spheres (e.g. latex colloids[4,13,60], mineral particles[7,61]), spheroids (e.g. carbon nanotubes[62], boehmite ellipsoids[25], starch granules[63]), polymeric chains (e.g. proteins[64], polysaccharides[65], fat molecules[66]) and patchy particles[38].

Calculation of the single-bond rigidity, κ_0, has been addressed by many authors. For long backbones, Kantor and Webman show that deformation occurs through angular rotation of backbone bonds[58]. Such resistance to bond bending implies the existence of non-central forces. These forces, especially for strong pair potentials, have been described as arising due to surface roughness, surface deformation, or steric stabilization[8,41]. Dinsmore et al. showed that fluctuations in fractal clusters were consistent with bond bending dynamics for strongly bonded gels[41]. Pantina and Furst successfully modeled κ_0 by applying Johnson-Kendall-Roberts (JKR) theory; the contact area generated by adhesive interactions supported bond flexure[67]. In this scenario, the bending rigidity tracks the strength of the inter-particle pair potential interactions, as described, in the present system, by the Derjaguin-Landau-Verwey-Overbeek (DLVO) potential. Pantina's calculations further suggest that computing κ_0 from thermal fluctuations of the colloid pair separation represents an upper bound to the actual bending constant[68]. Similar approaches have been used to model the steady shear viscosity of aggregating latex[69], the yield rheology of polystyrene and alumina gels[70], and the elasticity of dense depletion gels[71]. Here we pursue this approach to compute κ_0 from the thermal fluctuations of the colloid pair bond separation, weighted by the probability of different orientations for discoids.

Numerical values for the parameters in equation (1), as discussed earlier, are well known for DLCA sphere gels: $d_f \approx 1.85$, $\beta \approx 2.80 - 3.10$ and $f \approx 1 - 3$ [4,10,13,60]. However, these parameters may vary when the interparticle interactions and shape of constituent monomers differ from those of simple spheres. For example, from measurements of the dynamic structure factor,

Mohraz and co-workers found that gels consisting of rod-like particles displayed variations in both d_f and β with aspect ratio[14,28]. Simulations by West et al[72] showed that introducing angular rigidity in the gel backbone resulted in values of $\beta < 2$. Through theoretical fits to experimental data, Laxton and Berg reported a pre-factor of the modulus scaling with volume fraction that increased up to $\approx$ 50 for discotic clay gels[73]. Therefore, each of the parameters in equation (1) – d_f,β,f and κ_0 – may be aspect ratio dependent, a possibility we now explore. In the subsequent sections, we report independent, confocal microscopy derived, measurements of $d_f(r)$ and $\beta(r)$, theoretical calculations of $\kappa_0(r)$ and a least-squares determination of $f(r)$. Finally, using equation (1), we discuss how aspect ratio induced changes to these parameters act as multiplicative contributions to produce large shifts in discoid gel rheology, as reported in Figure 3.

3.4 Fractal dimension of the gel network

We measure d_f from confocal image volumes using box-counting image analysis, which utilizes spatial intensity data to quantify the dimensionality of the structure[35]. This method has previously been applied to quantify the microstructure of colloidal sphere gels[36,37,74], albumin gels[75], plasma protein gels[76] and soot aggregates[77]. The method is well-suited to the discoidal shape studied here. Briefly, the number of cubes $N(L)$ of size L required to cover the foreground pixels corresponding to the gel in confocal image volumes are computed at different values of the cube size (Figure 4(a)). The fractal dimension, d_f is then obtained from the power-law $N(L) = c_1 (L/I)^{-d_f}$. Here I is the image size and c_1 is a proportionality constant (c.f. Methods). For standard geometrical objects, the exponent of this power law will be equal to the Euclidean dimension of the system. Figure 4(b) shows the resulting log-log plot. The fitted lines corresponding to all r = 0.09 – 1.00 gels have power law slope of magnitude smaller than three, confirming the fractality of these structures.

Figure 4(c) shows that increasing particle shape anisotropy causes an increase in gel d_f. For sphere gels (r = 1), d_f = 1.86 $\pm$ 0.02, is consistent with the DLCA value of $d_f \approx$ 1.85. For discoid gels (r < 1), the value increases up to d_f = 2.04 $\pm$ 0.02 for the lowest aspect ratio (r = 0.09). This result is consistent with prior measurements for gels of rodlike particles (r > 1), which also reported an increase in gel d_f with increasing monomer anisotropy[14]. For instance, cluster gels made from r = 10 ellipsoids, which is complementary to the lowest aspect ratio discoid studied

here, had $d_f \sim 2.10$ [14]. Similarly, dilute gels of cellulose nanocrystals ($r = 20$) and clay platelets ($r = 0.05$) displayed $d_f \sim 2.1$ [78]and $d_f \sim 2.2$ [20] respectively. In Figure 4(b), the curves display an upward shift with aspect ratio, indicating an increase in c_1 with increasing discoidal anisotropy (inset Figure 4(c)).

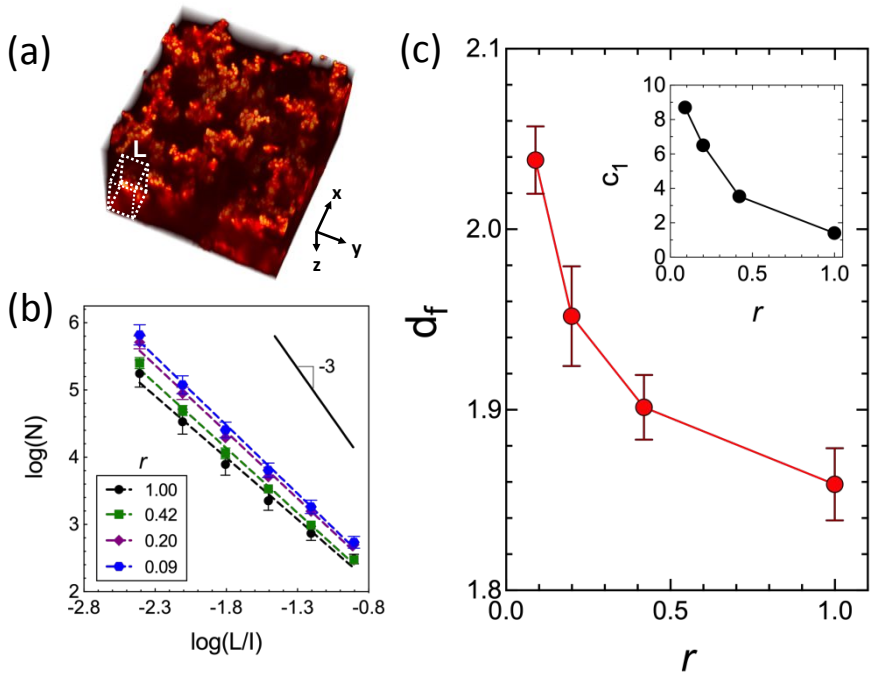

Figure 4. (a) 3D confocal visualization of a sphere colloidal gel. The white dotted lines illustrate a single cube in the box counting method. L is the resolution of the cube. (b) Log-log plot of number of cubes (N) vs. dimensionless cube size (L/I) for colloidal gels made from spheres ($r = 1$) and discoids ($r = 0.42$, 0.20 and 0.09). The dashed lines indicate a fit to the data as per the equation in the text. The solid line represents the Euclidean scaling of $N \sim L^{-3}$. (c) The gel fractal dimension, d_f and (inset) the prefactor c_1 as a function of aspect ratio r. The lines in (c) are included to guide the eye. Error bars for c_1 are small relative to the marker size.

The increase in network dimensionality indicates a deviation from the universality of DLCA aggregation[11]. Higher d_f indicate that discoids form denser cluster than spheres. The reason for the increased fractal dimension is attributed to the anisotropy in excluded volume as per simulations reported by Mohraz et al[14]. Physically, the increase in the proportionality constant c_1 as discoid anisotropy increases (aspect ratio decreases) indicates that the discoid fractal structures are more space filling relative to spheres at any length scale and controlling for fractal dimension. For instance, for a given box-size, the number of boxes required to completely fill the gel

microstructure is seven-fold higher for the case of r = 0.09 discoid gels than that required for sphere gels. The dependence of $c_1$on r thus shows that DLCA fractal structures produced from discoids are more compact than spheres.

3.5 Dimension and anisotropy of the gel backbone

We extract the gel backbone from confocal micrographs using skeletonization – a sequential thinning process that produces a voxel-thick skeletal backbone that encodes the topography and connectedness of the gel (c.f. Methods). It has been applied to measure backbone tortuosity of PMMA colloidal gels [44], pNIPAm colloidal gels[43] and nanoparticle aggregates[79]. From the gel skeleton, the backbone dimension, d_B is obtained from the relation between the length of the shortest path, l, between branch points on the skeleton and the end-to-end distance, r_E between them: $l = c_2 r_E^{d_B}$ [9,10]. The backbone anisotropy, ϵ is given as $r_\perp^2 = c_3 r_g^{2\epsilon}$ where, $r_\perp$ is the radius of gyration of the shortest path projected onto a plane perpendicular to its end-to-end axis and r_g is its center-of-mass radius of gyration[49,50]. Here, c_2 and c_3 are proportionality constants.

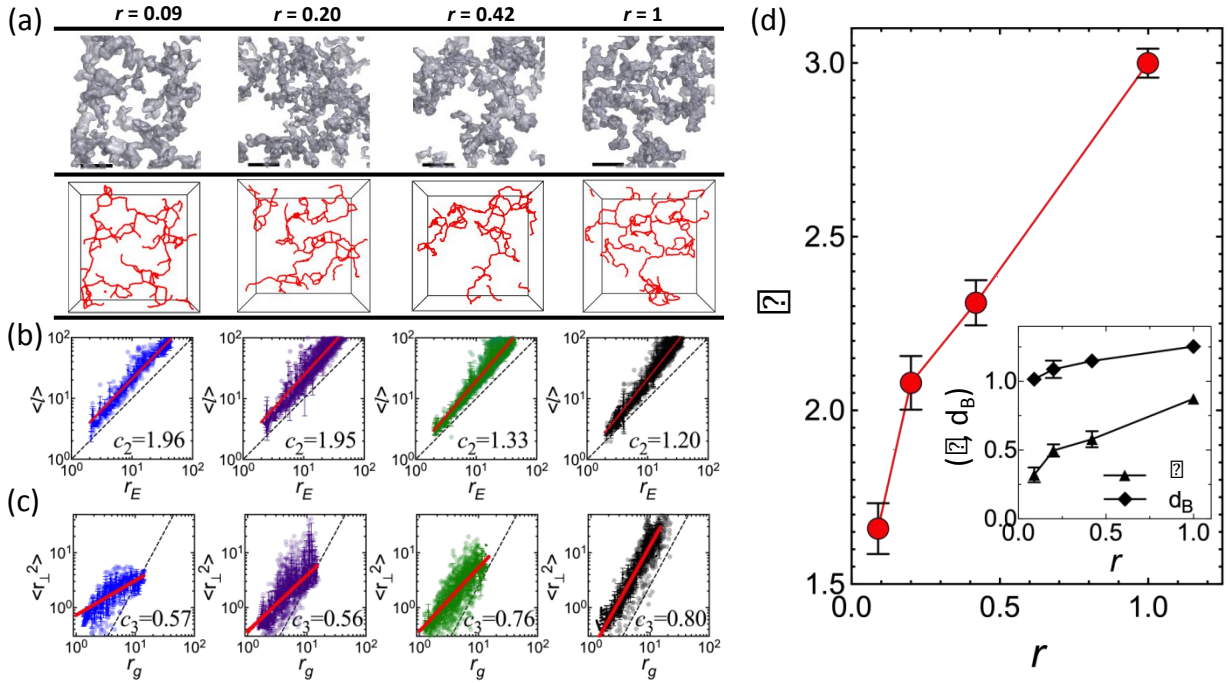

Figure 5. (a) Representative iso-surface rendering of binarized image volumes of the gels (top row) and their corresponding backbone skeleton (bottom row). The aspect ratios of the constituent particles are indicated on the top. Corresponding real-space confocal micrographs are shown in SI Figure S10. (b) Log-log plot of $\langle l \rangle$ versus r_E. (c) Log-log plot of $\langle r_\perp^2 \rangle$ versus r_g. The solid lines in (b) and (c) are respectively power-law fits: $\langle l \rangle = c_2 r_E^{d_B}$ and $\langle r_\perp^2 \rangle = c_3 r_g^{2\epsilon}$. The dashed lines indicate the case (b) d_B=1 and (c) ϵ =1. Values of the pre-factors c_2 and c_3 are included in the inset. (d) Dependence of β and (inset) d_B and ϵ on aspect ratio. Lines in (d) are drawn to guide the eye.

de Rooij et al identify the following limiting cases for the backbone shape parameters: $\epsilon = 1$ and $d_B = 5/3$ applies to an ideal self-avoiding isotropic chain, while $\epsilon = 0$ and $d_B = 1$ applies to a straight chain[8].

The skeletonization reveals the gel backbone microstructure as a sparse, interconnected network interspersed with voids (Figure 5(a)). Similar structures were also seen for gels formed by attractive microgel particles[44]. Figure 5(b)-(c) shows the corresponding plots of l vs r_E and $r_\perp^2$ vs r_g and the power-law fits to obtain d_B and ϵ, respectively. For sphere gels, the value $d_B = 1.26 \pm 0.03$ and $\epsilon = 0.80 \pm 0.02$ agrees well with the results of computer simulations (d_B = 1.30 and ϵ = 0.77)[9,80] and direct measurements ($d_B = 1.20$ and ϵ = 0.7)[10]. With increasing anisotropy, we find that d_B, ϵ (inset Figure 5(d)) and consequently the elasticity exponent, $\beta = 2\epsilon + d_B$ (Figure 5(d)) decrease, culminating at a value of β = 1.66 $\pm$ 0.08 for the lowest discoidal aspect ratio. A similar result was observed for rod gels where a value of $\beta \approx 1.20$ for r = 3.9 – 30.1 was measured by dynamic light scattering[28]. The constants c_2 and c_3 are approximately unity and relatively insensitive to r.

The elasticity exponent $\beta = 2\epsilon + d_B$determines the cluster spring constant[7]. Lower values of β for increased shape anisotropy, as reported in Figure 5, are due to decreases in both ϵ and d_B. The results show that the backbone of the discoidal clusters becomes progressively more anisotropic relative to spheres as the discoid aspect ratio decreases. To explain the decreased β of gels of anisometric colloids, Mohraz and Solomon made the connection between β and backbone angular rigidity[28]. They hypothesize that, in clusters of anisotropic particles, the presence of noncentral forces arising out of additional contacts per particle limit bond rotations. This limitation leads to gel backbones with large angular rigidity. By applying the Krall and Weitz theory for the dynamics of fractal cluster gels[4], they reported that this rigidity results in values of β that are lower than those for spheres. This hypothesis is supported by recent simulations showing that noncentral forces and additional contact points per particle lead to gels with less tortuous backbones[43] and higher shear modulus[81].

3.6 Interparticle bond spring constant

The interparticle bond strength, κ_0 is calculated from pair-potentials using the equipartition theorem, $\kappa_0 = k_B T/\left(\langle s^2\rangle - \langle s\rangle^2\right)$ [36,38,41,71]. Here, s is the surface-to-surface separation between

particle pairs and $\langle \cdot \rangle$ represents a Boltzmann weighted average[38]. That is, $\langle s \rangle = \int_0^\infty s e^{-U_{DLVO}(s)/k_BT} ds \Big/ \int_0^\infty e^{-U_{DLVO}(s)/k_BT} ds$. Here, k_B is the Boltzman constant and T is the temperature. The denominator in the expression for κ_0 thus represents an ensemble average over thermal fluctuations of the interparticle separation. For computing the Boltzmann averages, the interparticle pair potentials, $U_{DLVO}(s)$, are calculated using the DLVO theory as a sum of the screened electrostatic repulsion and van der Waals attraction, as per our prior work[38]. For discoids,

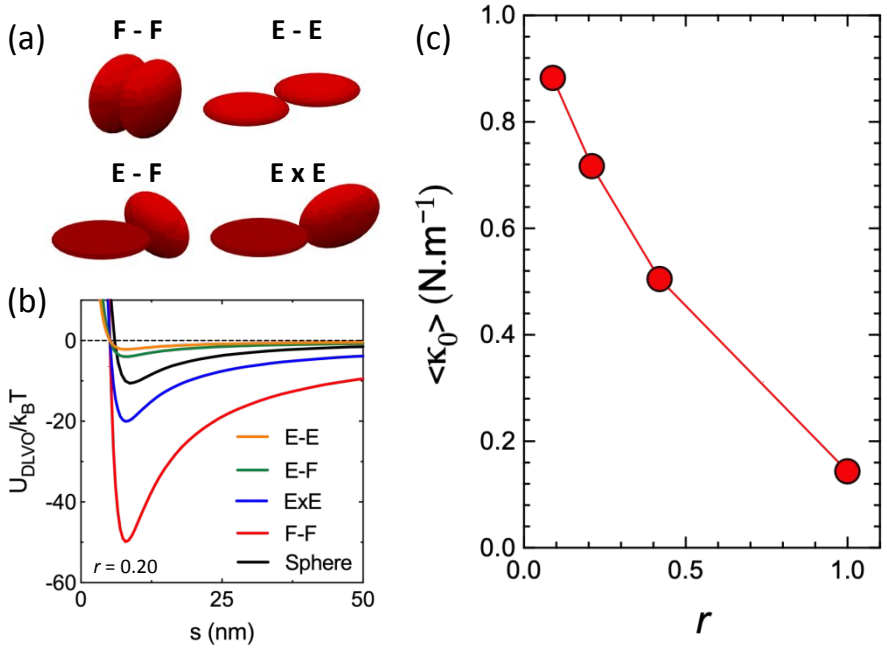

Figure 6. (a) Limiting cases of the pairwise orientation distribution of discoids: face-to-face (F-F), edge-to-edge (E-E), edge-to-face (E-F) and edge-on-edge (ExE). Discoids are not drawn to represent any specific aspect ratio used in this study. (b) DLVO pair-potential, U_{DLVO} normalized by k_BT for sphere pairs and discoid pairs corresponding to relative orientations shown in (a). Discoid pair-potentials are for the case $r = 0.20$. (c) Aspect ratio dependence of the orientationally averaged bond spring constant $\langle \kappa_0 \rangle$. Lines in (c) are drawn to guide the eye.

the dependence of the DLVO potential on the relative orientation of discoidal pairs are calculated using the expressions of Schiller et al[82].

For spheres, the interaction potential is isotropic; for discoids however, shape anisotropy introduces an anisotropy in the attractive pair potential[33]. To highlight the interaction anisotropy accorded by particle shape, four limiting configurations of discoid pairs, namely face-to-face (F-F), edge-to-edge (E-E), edge-to-face (E-F) and edge-on-edge (ExE) and their respective DLVO

pair-potentials, $U_{DLVO}(s)$ (calculated for r = 0.20) are shown in Figure 6(a)-(b). Supplemental Figure S11 plots the variation of bond energies for all possible pairwise alignments. We find that the interaction strength between discoidal pairs varies significantly with relative orientation (Figure 6(b)). F-F alignment results in the strongest attraction potential, significantly stronger than that between two spheres – while E-E and E-F alignments result in relatively weaker particle pair attractions. The stronger potential energy for F-F alignment was also observed in discoids interacting through depletion forces[33].

To calculate the interparticle bond strength between two discoidal colloids, we average over all relative orientations (Figure 6(a), SI Figure S11) weighted by their potential energy. That is, following Torres-Diaz et al, different orientational configurations are weighted by the Boltzmann distribution[83]. The assumption of the Boltzmann distribution is consistent with Hsiao et al[33]. In that study, the bond-angle distributions in clusters of attractive r = 0.5 discoids (which is intermediate to the range of r studied here) displayed a higher likelihood for the energetically stronger F-F configuration[33]. Figure 6(c) shows the degree to which the Boltzmann weighted, orientationally averaged bond strength, $\langle\kappa_0\rangle$ increases with shape anisotropy. For the lowest aspect ratio discoid, the bond strength increases by a factor of six relative to spheres. The increase in $\langle\kappa_0\rangle$ with monomer anisotropy indicates that, on average, discoidal bonds are stronger than spheres.

4. Discussion

The parameters of equation (1), except the proportionality constant $f(r)$, are available through Figures 4–6. We first test the performance of the model and the internal consistency of the different measurements by comparing the predicted scaling exponents with those determined by mechanical rheometry. Because of the independent confocal microscopy measurements, this comparison involves no adjustable parameters. The model predicts power law exponents, $(1+\beta)/(3-d_f)$ = 3.51 ± 0.13, 3.01 ± 0. 23, 2.90 ± 0.28 and 2.70 ± 0.25 for r = 1, 0.42, 0.20 and 0.09 respectively. These exponents can be compared to those derived from Figure 3. Both two-sample *t*-test and ANOVA comparing the experiment and model yields p = 0.9621, 0.7711, 0.3068 and 0.2059 for r = 1, 0.42, 0.2 and 0.09 respectively and p = 0.1179 across all conditions, indicating that the predicted exponents are statistically similar to the measured values. The comparison supports the application of the model to the discoidal gels; it further highlights the salience of the gel fractal and backbone dimensions to the rheological response. The differences in the $G' - \phi$

power law exponent seen in dilute anisometric colloidal gels vis-à-vis the value of ~ 3.5 seen for sphere gels is therefore due to shape mediated changes of the hierarchical fractal cluster microstructure of the gel network. Indeed, a recent study on dilute gels formed by nanocrystalline cellulose rods (r ~ 14) reported that the elastic modulus in these systems scaled as $G' \sim \phi^{2.70}$.[84] This exponent is in good agreement with that obtained by substituting d_f ~ 2.15 and β ~ 1.20 (as reported by Mohraz et al in ref [14] and [28], for rod gels of similar aspect ratio) in $(1+\beta)/(3-d_f) \approx 2.59$.

Figure 7(a) graphically compares the power law predictions of G' using equation (1) with the rheological measurements for each of the different aspect ratios gels, with excellent agreement. The proportionality constant, $f(r)$, determined through Figure 7(a) by least squares regression, yields f = 1.18 ± 0.14, 1.62 ± 0.60, 3.25 ± 1.10 and 8.55 ± 1.22 for r = 1, 0.4, 0.2 and 0.09 respectively (Figure 7(b)).

With the model and the independent characterizations in hand, we now specifically identify the set of multiplicative factors that generate the very large shifts seen in discoid gel rheology (Figure 3). At fixed G', this shift is as much as a factor of 15 at the lower volume fractions of the study. Returning to equation (1) the aspect ratio dependent rheological shift is a consequence of three multiplicative factors: $\phi^{\frac{1+\beta(r)}{3-d_f(r)}}$, $\langle \kappa_0 \rangle(r)$, and $f(r)$. The first term represents particle shape induced changes to the hierarchical microstructure of the gel, as characterized by the fractal dimension and backbone topography. These quantities mediate the contribution of volume fraction to gel modulus. To assess the relative contribution of this multiplicative factor to the shift in rheology, we select G' = 0.2 Pa as a reference value. The choice is recommended by the fact that measurements are available at this condition for each aspect ratio, and this modulus level is not an uncommon one for practical applications of colloidal gels. At this reference value, the multiplicative factor due to hierarchical microstructure accounts for 34% of the rheological shift between r = 1 and r = 0.09. The second multiplicative contribution is the effect of anisotropic pair potential on $\langle \kappa_0 \rangle(r)$. This multiplicative factor accounts for 23% of the shift in elastic modulus between r = 1 and r = 0.09. The third term is the aspect ratio dependent proportionality constant, $f(r)$, which accounts for the remaining 43% of the shift.

The physical origin of the aspect ratio dependence of $f(r)$ is of great interest since the greatest amount of the rheological shift is embodied in this quantity. We have examined the

physical factors affecting $f(r)$. At its root, these contributions involve the pre-factors that specify the quantitative relationships governing the density of the fractal network (d_f) and the backbone network (β, itself a function of ϵ and d_B). These prefactors are the constants c_1,c_2 and c_3, reported in Figures 4 and 5. Of these constants, by far the largest change is in c_1, and this constant was earlier identified as a measure of cluster compactness because it determines the absolute level of occupation of volumetric regions of the gel. We thus hypothesize that the third multiplicative factor affecting the rheological shift is cluster compactness. It is significant that each factor – hierarchical fractal microstructure, anisotropic pair potential, and cluster compactness – acts to shift the elastic rheology in the same direction. This alignment is the underlying origin of the enhanced effect of

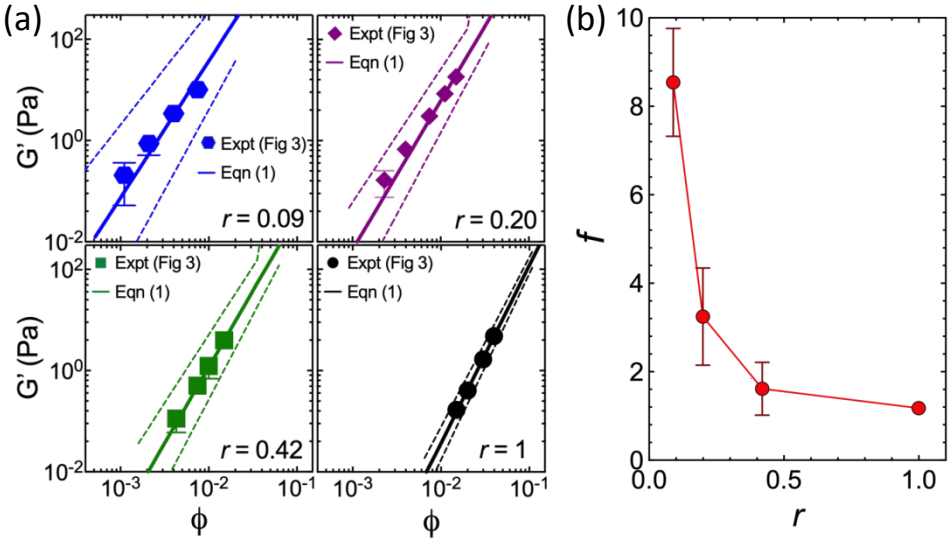

Figure 7. (a) Prediction of gel elastic modulus as function of volume fraction for sphere (r = 1) and discoid gels (r = 0.09, 0.20 and 0.42). The solid line represents predictions using equation (1) and dashed lines are confidence intervals obtained by propagation of errors in measured model parameters. (b) Aspect ratio dependence of proportionality constant, f.

particle shape anisotropy on the rheological response of dilute colloidal gels.

The results and the identification of the mechanistic origin of the shifted rheology in discoidal gels raise a number of questions and opportunities for future research. First, although the variation in f is here explained by changes to cluster compactness based as per the direct measurement of network connectivity (Figure 4,5), f could also include micromechanical contributions that would be of interest to explore. For instance, Kantor and Webman showed that the bending rigidity of the cluster backbone is inversely proportional to the number of flexible bonds (pivot points[10]) in the chain[58]. If a portion of the backbone is locally rigid (i.e. locally

arrested aggregates[71]), the effective spring constant would increase proportionally. This increase would in turn affect the magnitude of f. Therefore, probing the aspect ratio dependence of the density of angularly arrested bonds and its role in determining the macroscopic gel elasticity is suggested. An alternative micromechanical effect on f could arise from the role of bond-bending mechanics in determining the single-bond rigidity κ_0 itself. As discussed earlier, Pantina and Furst showed that the bending dynamics of a linear chain of spherical colloids can be quantitatively predicted by calculating κ_0 using the JKR theory for interparticle adhesion. This approach also invokes DLVO interactions; however, in this case their contribution is mediated by the bond contact area[67]. Application of their theory for a pair of attractive polystyrene spheres suggests that the bond-bending spring constant in this case is higher than the value plotted in Figure 6 by a factor of ≈ 4. This shift is comparable to the variability in f plotted in Figure 7(b). Therefore, future work to compare the JKR prediction for the r dependence[85] of κ_0 to the DLVO predictions in Figure 6 could determine if f harbors a hidden contribution of bending rigidity to gel elasticity[86].

Second, Figure 3 indicates that aspect ratio effects become progressively more pronounced as volume fraction decreases. The slower growth in G' with ϕ for $r < 1$ (as observable from the aspect ratio dependence of Π) implies that below a specific transition concentration – which for this system we would extrapolate to be about $\phi \sim 0.2$ – G' of discoid gels will always be higher than that of spheres. This observation coincides with prior results for rod gels[21]. The transition concentration likely coincides with the transition to fractality in the gels, which earlier has been discussed to occur at around $\phi \sim 0.1$ and below[87]. Identifying this transition concentration more specifically for anisotropic colloidal gels would identify the design space in which the multiplicate factors identified in this paper are available to formulators to achieve particular values of gel elasticity.

Third, although this work has addressed linear rheology, other non-linear rheological quantities – especially the yield stress and yield strain – warrant study. In their modeling, Shih et al show that the multiplicative factors reported in this study also impact yield rheology[7,8]. For instance, the gel yield stress is given to be proportional to $\kappa_0 \phi^{(2+\epsilon)/(3-d_f)}$; from Figures 4 – 6, at a characteristic concentration of $\phi = 0.01$, this dependency suggests that the yield stress in $r = 0.09$ discoid gels would be at least 20-fold higher than that of sphere gels. This observation is consistent with measurements for boehmite rod gels, where, increasing the rod aspect ratio was found to

generate as much as a factor of ~15 increase in the gel yield stress[21]. Additional study of non-linear rheological properties is warranted because they affect performance properties such paint application and formulation stability[2].

Fourth, the rheology of dilute gels made from a number of anisotropic materials (e.g., graphene oxide [23,88], laponite [20] and, MXenes[24]) have likewise been studied. Because of their anisometric shape, the rheology, flow, and mechanics of these materials can be predicted by means of the modeling and parametrization developed here[27]. Specifically, at dilute concentrations and with attractive pair potentials, these building blocks form fractal, percolating networks with fractal dimension[20] and rheology[24] shifted relative to isotropic spheres. However, early efforts to tune and design the rheology of these materials [23,24,88,89], have proceeded phenomenologically, and without recognition of the specific mechanisms revealed here that multiplicatively determine rheology in these systems. Therefore, the development of tools such as processability charts and printability maps in fields such as nanocomposite processing, additive manufacturing [23] and hydrogel formulation [89] can be informed by utilization of the three multiplicative factors identified in this study. Moreover, the structure and rheology of aggregating discotic clay particles has been studied extensively. In such systems, the material viscoelasticity is driven by the particles self-assembly into an intriguing house-of-cards network. Their rheology has been described using the well-known Chambon and Winter criteria for gelation [20]. Contrastingly, for the discotic latex particles used in this study, we instead observe a fractal network organization and consequently, show that their gel rheology can be modeled using theories for fractal network elasticity. Fundamentally, it would therefore be worthwhile to study the topographical differences between the latter two structures – that could for instance be derived through the backbone skeletonization analysis presented here – and how such differences, for instance a transition between the two types of microstructures, act to control the material viscoelasticity. Such fundamental understanding would better support the utilization of anisotropic particles for efficient material design.

Fifth, by demonstrating how and why shape anisotropic particles can be self-assembled to produce highly elastic gels at low volume fractions, this study suggests new directions for tuning the rheology of gels. Although the present worked identified the multiplicative factors for the case discoids, these factors are generally applicable. For example, they could potentially be used to produce gels from particles of intricate shape that were selected to leverage the factors of hierarchical structure, anisotropic pair potential, and cluster compactness. Such structures could

conceivably be more efficient at generating elasticity at low volume fractions than the discoidal shape studied here. This study's identification of the three independent, multiplicative factors therefore opens directions for gel design that are more specifically grounded in the physics of fractal structure, anisotropy, and self-assembly than previously available.

5. Conclusion

In conclusion, universal microstructural features of dilute gels of spherical colloids limit their rheological design space. We have shown that changing the particle shape from sphere to discoid produces the same elasticity at only one-fifteenth the volume fraction and that the volume fraction dependence of elastic modulus in discoidal gels is greatly shifted from that seen for spheres. The degree of shift is tunable through the particle aspect ratio. Moreover, the mechanism for this large shift has been revealed to be the consequence of a combination of independent factors governed by particle shape induced changes to the fractal cluster microstructure. These findings can be applied to optimize gel rheology in industries such as food, cosmetics, pharmaceuticals, and coatings; they suggest new avenues to control and tune colloidal gel elasticity using particle anisotropy.

6. Author Contributions

P.K.K. and M.G. synthesized the colloidal particles and carried out the experiments. P.K.K., M.J.S. and M.G. designed the project, analyzed the data, and wrote the manuscript. All authors discussed and commented on the manuscript.

7. Conflicts of Interest

The authors declare no competing interests

8. Acknowledgements

Support for this study was provided by the National Science Foundation (No. CBET-1702418). For scanning electron microscopy, the authors acknowledge the financial support of the University of Michigan College of Engineering and NSF grant #DMR-1625671, and the technical support from the Michigan Center for Materials Characterization.

9. References

1 P. J. Lu and D. A. Weitz, *Annu. Rev. Condens. Matter Phys.*, 2013, **4**, 217–233.

2 T. F. Tadros, *Colloids in Paints*, Wiley-VCH Verlag GmbH & Co. KGaA, Weinheim, Germany, 2010.

3 T. F. Tadros, *Colloid Stability and Application in Pharmacy*, Wiley-VCH Verlag GmbH & Co. KGaA, Weinheim, Germany, 2007, vol. 3.

4 A. H. Krall and D. A. Weitz, *Phys. Rev. Lett.*, 1998, **80**, 778–781.

5 H. Tsurusawa, M. Leocmach, J. Russo and H. Tanaka, *Sci. Adv.*, 2019, **5**, eaav6090.

6 P. J. Lu, E. Zaccarelli, F. Ciulla, A. B. Schofield, F. Sciortino and D. A. Weitz, *Nature*, 2008, **453**, 499–503.

7 W.-H. Shih, W. Y. Shih, S.-I. Kim, J. Liu and I. A. Aksay, *Phys. Rev. A*, 1990, **42**, 4772–4779.

8 R. de Rooij, D. van den Ende, M. H. G. Duits and J. Mellema, *Phys. Rev. E*, 1994, **49**, 3038–3049.

9 P. Meakin, I. Majid, S. Havlin and H. E. Stanley, *J. Phys. A. Math. Gen.*, 1984, **17**, L975–L981.

10 A. D. Dinsmore and D. A. Weitz, *J. Phys. Condens. Matter*, 2002, **14**, 303.

11 M. Y. Lin, H. M. Lindsay, D. A. Weitz, R. C. Ball, R. Klein and P. Meakin, *Nature*, 1989, **339**, 360–362.

12 J. H. Cho, R. Cerbino and I. Bischofberger, *Phys. Rev. Lett.*, 2020, **124**, 088005.

13 S. Romer, H. Bissig, P. Schurtenberger and F. Scheffold, *EPL*, 2014, **108**, 48006.

14 A. Mohraz, D. B. Moler, R. M. Ziff and M. J. Solomon, *Phys. Rev. Lett.*, 2004, **92**, 155503.

15 T. Gisler, R. C. Ball and D. A. Weitz, *Phys. Rev. Lett.*, 1999, **82**, 1064–1067.

16 R. Buscall, P. D. A. Mills, J. W. Goodwin and D. W. Lawson, *J. Chem. Soc. Faraday Trans. 1 Phys. Chem. Condens. Phases*, 1988, **84**, 4249.

17 M. Chen and W. . Russel, *J. Colloid Interface Sci.*, 1991, **141**, 564–577.

18 H. Wu, J. Xie and M. Morbidelli, *Soft Matter*, 2013, **9**, 4437.

19 J. P. Pantina and E. M. Furst, *Langmuir*, 2006, **22**, 5282–5288.

20 S. Jatav and Y. M. Joshi, *Faraday Discuss.*, 2016, **186**, 199–213.

21 A. Wierenga, A. P. Philipse, H. N. W. Lekkerkerker and D. V. Boger, *Langmuir*, 1998,

14, 55–65.

22 N. Krishna Reddy, Z. Zhang, M. Paul Lettinga, J. K. G. Dhont and J. Vermant, *J. Rheol.*, 2012, **56**, 1153–1174.

23 A. Corker, H. C.-H. Ng, R. J. Poole and E. García-Tuñón, *Soft Matter*, 2019, **15**, 1444–1456.

24 B. Akuzum, K. Maleski, B. Anasori, P. Lelyukh, N. J. Alvarez, E. C. Kumbur and Y. Gogotsi, *ACS Nano*, 2018, **12**, 2685–2694.

25 A. Mohraz and M. J. Solomon, *J. Rheol.*, 2005, **49**, 657–681.

26 S. Lazzari, L. Nicoud, B. Jaquet, M. Lattuada and M. Morbidelli, *Adv. Colloid Interface Sci.*, 2016, **235**, 1–13.

27 M. J. Solomon and P. T. Spicer, *Soft Matter*, 2010, **6**, 1391.

28 A. Mohraz and M. J. Solomon, *J. Colloid Interface Sci.*, 2006, **300**, 155–162.

29 A. P. Philipse and A. M. Wierenga, *Langmuir*, 1998, **14**, 49–54.

30 S. J. Ahn, K. H. Ahn and S. J. Lee, *Colloid Polym. Sci.*, 2016, **294**, 859–867.

31 M. Ganesan and M. J. Solomon, *Soft Matter*, 2017, **13**, 3768–3776.

32 B. Madivala, J. Fransaer and J. Vermant, *Langmuir*, 2009, **25**, 2718–2728.

33 L. C. Hsiao, B. A. Schultz, J. Glaser, M. Engel, M. E. Szakasits, S. C. Glotzer and M. J. Solomon, *Nat. Commun.*, 2015, **6**, 8507.

34 M. Carpineti, F. Ferri, M. Giglio, E. Paganini and U. Perini, *Phys. Rev. A*, 1990, **42**, 7347–7354.

35 A. Thill, S. Veerapaneni, B. Simon, M. Wiesner, J. Y. Bottero and D. Snidaro, *J. Colloid Interface Sci.*, 1998, **204**, 357–362.

36 J. Ruiz-Franco, F. Camerin, N. Gnan and E. Zaccarelli, *Phys. Rev. Mater.*, 2020, **4**, 045601.

37 C. J. Dibble, M. Kogan and M. J. Solomon, *Phys. Rev. E*, 2006, **74**, 041403.

38 K. T. Saud, M. Ganesan and M. J. Solomon, *J. Rheol.*, 2021, **65**, 225–239.

39 D. B. Allan, T. Caswell, N. C. Keim, C. M. van Der Wel and R. W. Verweij, 2021.

40 V. Ramasubramani, B. D. Dice, E. S. Harper, M. P. Spellings, J. A. Anderson and S. C. Glotzer, *Comput. Phys. Commun.*, 2020, **254**, 107275.

41 A. D. Dinsmore, V. Prasad, I. Y. Wong and D. A. Weitz, *Phys. Rev. Lett.*, 2006, **96**, 1–6.

42 M. Lattuada, H. Wu, A. Hasmy and M. Morbidelli, *Langmuir*, 2003, **19**, 6312–6316.

43 J. N. Immink, J. J. E. Maris, P. Schurtenberger and J. Stenhammar, *Langmuir*, 2020, **36**, 419–425.

44 J. N. Immink, J. J. E. Maris, R. F. Capellmann, S. U. Egelhaaf, P. Schurtenberger and J. Stenhammar, *Soft Matter*, 2021, **17**, 8354–8362.

45 P. Kollmannsberger, M. Kerschnitzki, F. Repp, W. Wagermaier, R. Weinkamer and P. Fratzl, *New J. Phys.*, 2017, **19**, 073019.

46 N. Otsu, *IEEE Trans. Syst. Man. Cybern.*, 1979, **9**, 62–66.

47 M. Kerschnitzki, P. Kollmannsberger, M. Burghammer, G. N. Duda, R. Weinkamer, W. Wagermaier and P. Fratzl, *J. Bone Miner. Res.*, 2013, **28**, 1837–1845.

48 P. Kollmannsberger, 2018.

49 A. A. Potanin, *J. Colloid Interface Sci.*, 1991, **145**, 140–157.

50 A. A. Potanin, *J. Chem. Phys.*, 1992, **96**, 9191–9200.

51 R. H. Ewoldt, M. T. Johnston and L. M. Caretta, in *Complex Fluids in Biological Systems*, ed. S. E. Spagnolie, Springer, New York, NY, 2015, pp. 207–241.

52 L. C. Hsiao, R. S. Newman, S. C. Glotzer and M. J. Solomon, *Proc. Natl. Acad. Sci.*, 2012, **109**, 16029–16034.

53 B. Ruzicka and E. Zaccarelli, *Soft Matter*, 2011, **7**, 1268–1286.

54 M. Diez-Silva, M. Dao, J. Han, C.-T. Lim and S. Suresh, *MRS Bull.*, 2010, **35**, 382–388.

55 M. Das, L. Chambon, Z. Varga, M. Vamvakaki, J. W. Swan and G. Petekidis, *Soft Matter*, 2021, **17**, 1232–1245.

56 R. Buscall, *Colloids and Surfaces*, 1982, **5**, 269–283.

57 R. Buscall, P. D. A. Mills, R. F. Stewart, D. Sutton, L. R. White and G. E. Yates, *J. Nonnewton. Fluid Mech.*, 1987, **24**, 183–202.

58 Y. Kantor and I. Webman, *Phys. Rev. Lett.*, 1984, **52**, 1891–1894.

59 J. R. Rothenbuhler, J.-R. Huang, B. A. DiDonna, A. J. Levine and T. G. Mason, *Soft Matter*, 2009, **5**, 3639.

60 P. B. Laxton and J. C. Berg, *Colloids Surfaces A Physicochem. Eng. Asp.*, 2007, **301**, 137–140.

61 T. Liberto, M. Le Merrer, C. Barentin, M. Bellotto and J. Colombani, *Soft Matter*, 2017, **13**, 2014–2023.

62 E. K. Hobbie, *Rheol. Acta*, 2010, **49**, 323–334.

63 M. A. Rao, *Rheology of foods, semisolid, and solid foods. Principles and Aplications*, Springer New York, New York, NY, Third., 2014.

64 M. Mellema, J. H. J. van Opheusden and T. van Vliet, *J. Rheol.*, 2002, **46**, 11–29.

65 Y. Cao and R. Mezzenga, *Nat. Food*, 2020, **1**, 106–118.

66 S. S. Narine and A. G. Marangoni, *Phys. Rev. E*, 1999, **60**, 6991–7000.

67 J. P. Pantina and E. M. Furst, *Phys. Rev. Lett.*, 2005, **94**, 138301.

68 J. P. Pantina, University of Delaware, 2006.

69 R. De Rooij, A. A. Potanin, D. Van Den Ende and J. Mellema, *J. Chem. Phys.*, 1993, **99**, 9213–9223.

70 W. Y. Shih, W.-H. Shih and I. A. Aksay, *J. Am. Ceram. Soc.*, 2004, **82**, 616–624.

71 K. A. Whitaker, Z. Varga, L. C. Hsiao, M. J. Solomon, J. W. Swan and E. M. Furst, *Nat. Commun.*, 2019, **10**, 2237.

72 A. H. L. West, J. R. Melrose and R. C. Ball, *Phys. Rev. E*, 1994, **49**, 4237–4249.

73 P. B. Laxton and J. C. Berg, *J. Colloid Interface Sci.*, 2006, **296**, 749–755.

74 A. Boromand, S. Jamali and J. M. Maia, *Soft Matter*, 2017, **13**, 458–473.

75 T. Hagiwara, H. Kumagai and K. Nakamura, *Food Hydrocoll.*, 1998, **12**, 29–36.

76 E. Dàvila and D. Parés, *Food Hydrocoll.*, 2007, **21**, 147–153.

77 M. Altenhoff, S. Aßmann, C. Teige, F. J. T. Huber and S. Will, *J. Aerosol Sci.*, 2020, **139**, 105470.

78 F. Cherhal, F. Cousin and I. Capron, *Langmuir*, 2015, **31**, 5596–5602.

79 B. A. Legg, M. Zhu, L. R. Comolli, B. Gilbert and J. F. Banfield, *Langmuir*, 2014, **30**, 9931–9940.

80 Z. Rácz and M. Plischke, *Phys. Rev. A*, 1985, **31**, 985–994.

81 H. T. Nguyen, A. L. Graham, P. H. Koenig and L. D. Gelb, *Soft Matter*, 2020, **16**, 256–269.

82 P. Schiller, S. Krüger, M. Wahab and H.-J. Mögel, *Langmuir*, 2011, **27**, 10429–10437.

83 I. Torres-Díaz, B. Rupp, Y. Yang and M. A. Bevan, *Soft Matter*, 2018, **14**, 934–944.

84 Y. Xu, A. D. Atrens and J. R. Stokes, *J. Colloid Interface Sci.*, 2017, **496**, 130–140.

85 K. L. Johnson and J. A. Greenwood, *J. Phys. D. Appl. Phys.*, 2005, **38**, 1042–1046.

86 F. Bonacci, X. Chateau, E. M. Furst, J. Fusier, J. Goyon and A. Lemaître, *Nat. Mater.*, 2020, **19**, 775–780.

87 P. Varadan and M. J. Solomon, *Langmuir*, 2001, **17**, 2918–2929.

88 S. Naficy, R. Jalili, S. H. Aboutalebi, R. A. Gorkin III, K. Konstantinov, P. C. Innis, G. M. Spinks, P. Poulin and G. G. Wallace, *Mater. Horiz.*, 2014, **1**, 326–331.

89 S. Unterman, L. F. Charles, S. E. Strecker, D. Kramarenko, D. Pivovarchik, E. R. Edelman and N. Artzi, *ACS Nano*, 2017, **11**, 2598–2610.